Research papers

Can temperature be a low-cost tracer for modelling water age distributions in a karst catchment?

Zhicai Zhang [a,d,*], Xian Wang [a], Xi Chen [b], Yongyu Xie [a], Qinbo Cheng [a], Qing He [a], Tao Peng [c,d], Bo Chen [d], Chris Soulsby [e]

[a] College of Hydrology and Water Resources, Hohai University, Nanjing 210098, China
[b] Institute of Surface-Earth System Science, School of Earth System Science, Tianjin University, Tianjin 300072, China
[c] Institute of Geochemistry Chinese Academy of Sciences, Guiyang 550081, China
[d] Puding Karst Ecosystem Research Station, Chinese Academy of Sciences, Puding 562100, China
[e] School of Geosciences, University of Aberdeen, Aberdeen AB24 3UF, United Kingdom

ABSTRACT

To investigate the feasibility of using temperature for tracking rainfall-runoff processes in karst catchments, this study developed a tracer-aided conceptual model using temperature as a tracer by coupling water and heat transport processes at the catchment scale. The model was calibrated and validated using hourly hydrometeorological and temperature data from a 1.25 km^2 karst catchment in south-western China. The results showed that the model was able to capture the water flux and temperature dynamics of different landscape units in the karst catchment. Utilizing this framework, the model delineated the flux age distribution within different landscape units, as well as the overall water transit times through the catchment. The average flux ages were determined to be approximately 80 days for the hillslope unit, 452 days for the slow flow system, and 260 days for the fast flow regime within the depression areas. These estimations align broadly with those acquired using stable isotopes as tracers. Comparative analysis revealed that the flux age distributions derived from both temperature and isotopic tracers exhibited analogous patterns at the catchment outlet and across the hillslope compartments. However, the simulations based on temperature hinted at a heightened proportion of exceedingly young and decidedly old water in the outflow, alluding to a potential overestimation of these extreme age classes by the temperature-tracer model. From the temperature-simulated transit time distribution, about 31 % of the precipitation entering during the study period have left the catchment within 3 years, and a notable proportion of rain water was either stored in the aquifer or lost through evapotranspiration. The general characteristics of the transit time distribution simulated using temperature was similar with that simulated using isotopes, though a higher proportion of precipitation being drained by fast flows was inferred from the transit time distribution simulated using temperature. Collectively, our study demonstrated that temperature can serve as a cost-effective tracer for modelling of water age distributions and associated hydrological processes in karst catchments.

1. Introduction

As descriptors of hydrological function, e.g. flux age distributions and transit time distributions (TTDs), can provide conceptual, integrated understanding of the mixing processes and flow paths that transform precipitation inputs to runoff at catchment outlets (Botter, 2012; Kirchner et al., 2000; McDonnell and Beven, 2014; Soulsby et al., 2015; van der Velde et al., 2015). The time-scale functions can analyse the dynamics of storage-flux-age response time (RT) interactions and have

been used to investigate patterns of hillslope/catchment response and stream water chemical dynamics (Botter et al., 2011; Hrachowitz et al., 2013; Rinaldo et al., 2015). Particularly, incorporating the functions in hydrological models can provide new insights into the hydrological processes in karst catchments with high spatial heterogeneity (Rusjan et al., 2019; Zhang et al., 2021a; Serène et al., 2022).

To better understanding the time-scale functions on hydrological processes of catchments, tracer sampling is often necessary to capture high variability of hydrograph and tracer concentration in response to

rainfall (Kirchner et al., 2004; Birkel et al., 2012). In many catchments, high spatio-temporal resolution tracer data are a prerequisite for accurately characterising the complexity and heterogeneity of catchment responses across a range of timescales. However, in many cases, such detail data are unavailable. Although low temporal resolution sampling (e.g. weekly or even monthly) is still often adopted in tracer-based modelling (Borriero et al., 2023; Yang et al., 2023) to investigate hydrological function during dry seasons or over longer time scales, it is unable to track changes in water flow at smaller time scales and cannot identify rapid hydrological changes. This limitation is particularly pronounced for karst environment with rapid rainfall-runoff responses (Zhang et al., 2019).

The most commonly tracers used in tracer-aided hydrological models include stable isotopes (e.g. ^{18}O and ^{2}H), electrical conductivity (Lazo et al., 2023), chemical ions of chloride, and alkalinity (Capell et al., 2012; Benettin et al., 2013), and fluorobenzoic tracers (Asadollahi et al., 2020). However, conducting long-term high spatio-temporal resolution sampling and analysis for such tracers is logistically challenging in terms of high financial costs for sampling, and laboratory analysis of water samples. Compared to these tracers, temperature is a much cheaper alternative for long-term, high spatio-temporal resolution monitoring due to the advantages of simple detection technology and low maintenance costs, which can be monitored online at high temporal resolution with inexpensive sensors (Webb et al., 2008; Jackson et al., 2016; Simon et al., 2022). Additionally, temperature monitoring has the merit of having low environmental impacts involving small, inobtrusive technology and infrastructure, which requires minimal-disturbance, non-destructive installation and non-pollution. These features also make it advantageous for distributed monitoring purposes at the catchment scale.

Temperature as a non-conservative tracer may limit its application for tracking rainfall-runoff processes. As reported by Luhmann et al. (2012), the nonconservative nature of temperature could produce a lagged and damped thermal signal, compared with that from the conservative tracers. However, this shortage can be overcome by incorporating an additional function that describes water exchanged heat with the soil and rock along the flow path in the models. The increase of nonconservative traces and correspondingly sophisticated representations of hydrochemical processes are also executed in coupled water-solute models using reactive substances of nitrogen and carbon (Birkel et al., 2020; Zhang et al., 2020a; Wu et al., 2022). In such situations, one of key necessary steps is to identify the functions of tracers on dominant hydrochemical processes, which can acknowledge whether the added information is useful in fitting nonconservative parameters (e.g., Gooseff and McGlynn, 2005), constraining models and reducing parameter uncertainty (Kelleher and Ward, 2019). For instance, Luhmann et al. (2012) found that water temperature signals provide potential constraints on flow path characteristics of the heat advection–dispersion equation because the karst conduit geometry is correlation with the rate of heat exchange between water and rock. Furthermore, the combination of hydraulic response and conservative and nonconservative tracers can illustrate unique hydrochemical processes and reduce parameter uncertainty (Luhmann et al. 2012; Kelleher and Ward, 2019).

The main aim of this study is to develop a tracer-aided conceptual hydrological model using available hydrometeorological and temperature observation data for tracking rainfall-runoff processes in a karst catchment in south-western China. The model is used to simulate the water age dynamics of the catchment. The simulated water age distributions in different units of the catchment are compared with those of previous tracer aid-modelling with isotope data. The comparison delineates two specific research questions: (1) can temperature, as a non-conservative tracer, be reliable in simulating water age distributions in karst catchments? (2) can the simulated water age distributions well elucidate hydrological and heat dynamics within various units of a karst catchment?

2. Study catchment and data

2.1. Study catchment

The study catchment of Chenqi, with an area of 1.25 km^2, is located in the Puding Karst Ecohydrological Observation Station in Guizhou Province of south-western China (Fig. 1). The area has a subtropical monsoon climate characterized by high humidity and abundant rainfall during the wet season from May to October. The Chenqi catchment is a typical cockpit karst landscape, with cone-shaped mountains surrounding a flat depression. The elevation ranges from 1340 to 1530 m, with the depression area of 0.37 km^2 and the mountainous area of 0.88 km^2. Within the depression, there is an underground conduit which serves as the main drainage for the catchment.

The lithology in the Chenqi catchment mainly consists of marl, thick limestone, thin limestone, and dolomite (Fig. 1). The soil layer is shallow in this area, and in most area on the hillslope is less than 30 cm thick. In contrast, the depression has a relatively thicker soil, generally more than 2 m deep. Soil cover is irregular, especially in steeper hillslope areas, and the exposed rock ratio in the catchment ranges from 0.1 to 0.3. Forests, shrubs, and sloping cultivated lands are mainly distributed on the slopes of the catchment, while the depression is predominantly farmland. The thickness of the epikarst layer in this catchment is estimated to be approximately 10 m and the average porosity is about 5 % (Zhang et al., 2013).

2.2. Hydrometric and temperature data

Water levels and temperatures are monitored at sites with v-notch weirs at the catchment outlet (underground conduit outlet) and a spring on the eastern hillslope (HS spring in Fig. 1), using HOBO U20 water level loggers, Onset Corporation, USA (instrument precision ± 0.3 cm for water level and ± 0.5℃ for temperature). The water levels are converted into discharge using weir flow formulas. An automatic weather station is installed on the southern hillslope of the catchment to observe meteorological conditions such as rainfall, air temperature, radiation, wind speed, and humidity. In the depression, there are four wells (W1, W3, W4, and W5 in Fig. 1) for groundwater level and temperature monitoring, which are also equipped with HOBO U20 water level loggers. These wells are in a phreatic aquifer, with depth to ground surface of 35, 23, 13, and 16 m, respectively. Local flows at various depths can enter well through the well screening installed over the whole depth for each of the wells. Soil temperature automatic monitoring probes (HOBO H21 with instrument precision ± 0.2℃) are installed on the north-eastern hillslope of the catchment at depths of 20 cm and 40 cm. The logging time interval for all measurements is set to 15 min.

The data collection period ran from July 23, 2016 to October 31, 2019. Due to instrument malfunctions, some data were missing, such as the soil temperature at the depth of 40 cm after December 2018. During the winter drought period, there were a few times that flow discharges completely ceased at the catchment outlet (Fig. 2). From the observed time series, the response of discharge at the catchment outlet to rainfall was rapid and intense, exhibiting sharp variability in the hydrograph. Overall, the temperatures of the catchment outflow, HS spring flow, depression groundwater, and soil were closely related to changes in air temperature, all exhibiting significant seasonal variations but also short-term perturbations in response to rainfall events (Fig. 2). Compared to the catchment outflow temperature, the temperature of HS spring discharge showed more significant seasonal fluctuations. Over the study period, the pattern of soil temperature at 20 cm depth is consistent with that at 40 cm depth, likely related to the lower soil density and rapid vertical groundwater flow within the soil layer. The groundwater temperatures at different wells exhibited significant different responses to rainfall due to the spatial heterogeneity of the karst geological structure and water flows in the aquifer (Fig. 2). In some heavy rainfall events,
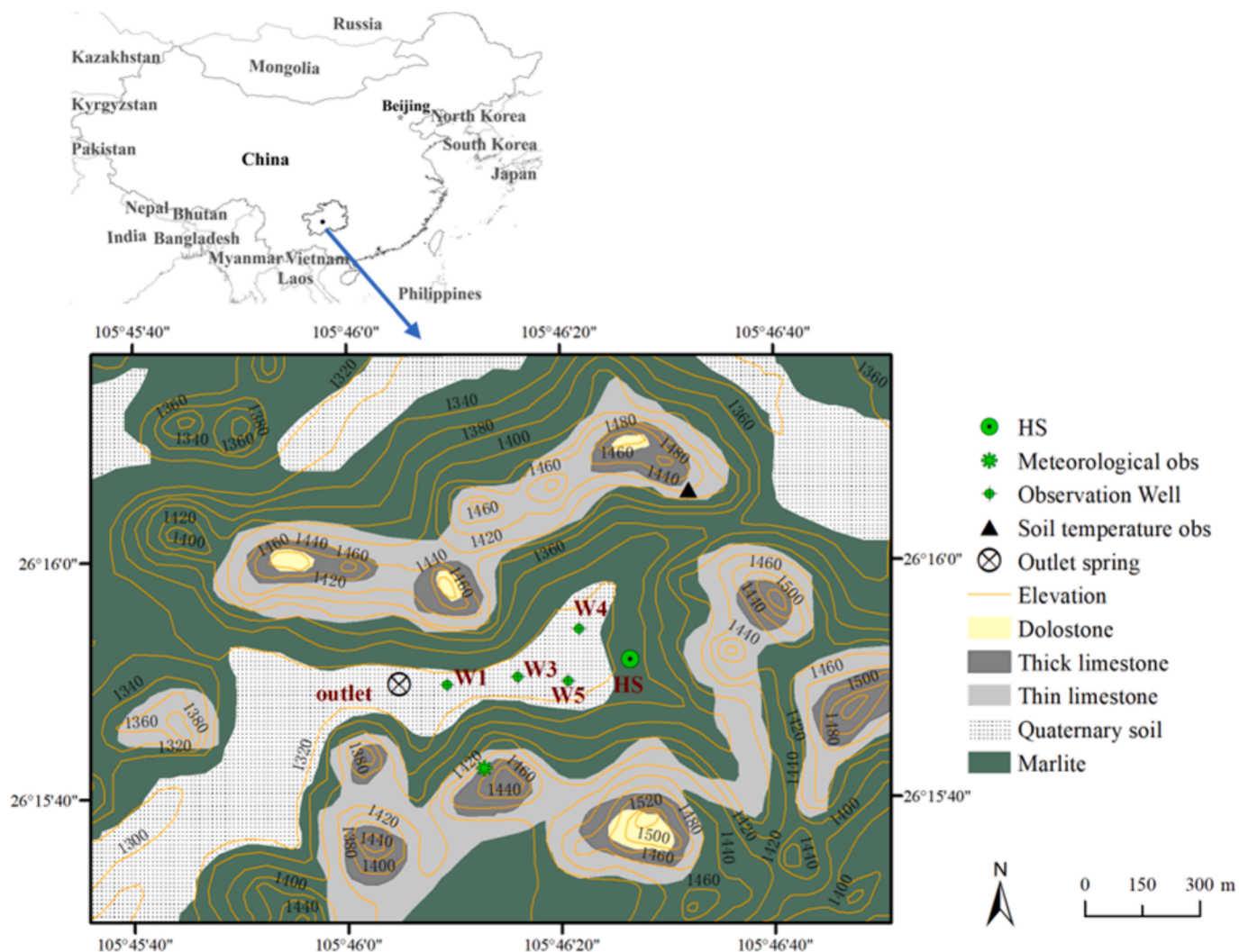
Fig. 1. Map of location, geology, geomorphology, and hydrological and temperature monitoring locations in Chenqi catchment.

surface water with higher temperatures rapidly entering the underground conduits and wells through sinkholes or large fractures, leading to a significant increase in temperatures at the catchment outlet and wells (Fig. 2). Additionally, we collected rainwater and measured rainwater temperature of 9 rainfall events during March ~ July in 2023, and observed the corresponding air temperature and rainwater temperature at the respective times. The rainwater temperature was lower than the air temperature for each event, with an average difference of 1.1 ℃, and the maximum and minimum differences being 1.7 and 0.5 ℃, respectively. Statistical characteristics of rainfall, discharge, and temperatures were summarized in Table 1.

3. Methodology

3.1. Modelling approaches

A conceptual tracer-aided hydrological model using stable isotopes as tracers has been established by Zhang et al., (2019). In the model, the catchment was divided into HS unit and depression units, and hydrological routings fast and slow flow reservoirs in the depression unit. To take into account the partial mixing of incoming water fluxes with stored water, a passive reservoir was added to the HS unit in the original model, which determined storage, mixing, and tracer transport without affecting the volume of water fluxes. Based on this framework, we coupled water and energy balance calculations to track water and heat

fluxes through each landscape unit and associated storages in the karst catchment. The heat module conceptualises a heat conduction-advection equation, which takes into account the heat transfer by conduction and advection within the karst hydrogeological system. According to temperature damping due to heat fluxes, water age distributions in various landscape units can be estimated according to model parameters determined by temperature damping caused by heat fluxes. The model structure and water-heat processes are conceptualised as shown in Fig. 3.

3.1.1. Hydrological simulation

The water balance of each unit and reservoirs was calculated as follows (Zhang et al., 2019):

$$\frac{dV_h}{dt} = P_h - ET_h - Q_{h-s} - Q_{h-f} \tag{1}$$

$$\frac{dV_s}{dt} = P_s - ET_s + Q_{h-s} - Q_e \tag{2}$$

$$\frac{dV_f}{dt} = P_f - ET_f + Q_{h-f} + Q_e - Q_f \tag{3}$$

where V represents a water storage, P is rainfall amount, and ET is evapotranspiration. The subscripts of h, s, f represent the HS unit, slow and fast reservoirs, respectively. Rainfall amount is distributed to HS
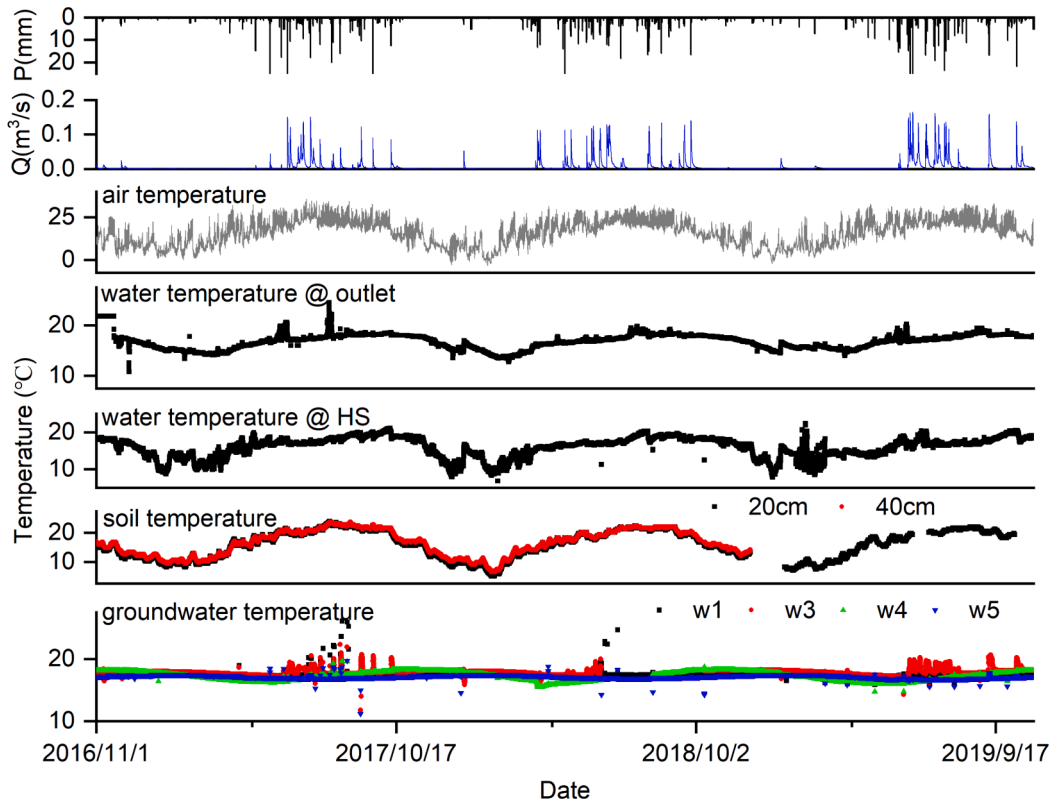
Fig. 2. Processes of rainfall, discharge, air temperature, soil temperature at 20 and 40 cm depth, and water temperature at HS spring, wells and outlet.

Table 1
Statistical characteristics of rainfall, discharge and temperatures during the study period.

Obs			Max	Min	Mean
Rainfall (mm)Discharge			44.9	0.0	0.1
(m³/s)			0.16	0	0.01
Temperature (℃)	Air		35.6	−3.3	16.1
	Outlet flow		24.5	10.8	17.1
	HS spring flow		22.4	6.9	16.2
	Soil	20 cm	24.0	5.0	16.3
		40 cm	23.6	6.6	16.9
	Well	#1	26.1	15.9	17.4
		#3	22.3	11.8	17.9
		#4	19.6	14.7	17.2
		#5	19.7	11.2	17.1

and depression units according to their respective areas, then the rainfall amounts infiltration into slow and fast flow (P_s and P_f) are estimated by the recharge coefficient of a (in Table 2). Q_f is flow discharge of fast reservoir, which also represents the conduit flow at the catchment outlet. Q_{h-s} and Q_{h-f} are water flows from HS unit to slow and fast reservoirs in depression, respectively. Q_e represents the flow exchanges between fast and slow reservoirs. The detailed descriptions of computations for each variable and the flow routing refer to Zhang et al., (2019).

3.1.2. Heat simulation

An energy balance for waters in any units or reservoirs (Fig. 3) can be expressed as: heat accumulation rate (Js^{-1}) = advective heat from flow in − advective heat from flow out + conductive heat from soil or rock. The heat transport along flow paths in the HS unit are calculated as:

$$\frac{d\rho_W c_w(T_h V_h)}{dt} = U_{cv\_h} + U_{cd\_h} \tag{4}$$

where T_h is the temperature of the bulk water flowing in the hillslope (℃); U_{cv} and U_{cd} are the net heat flux of advection and conduction, respectively; ρ and c represent density (kg m^{-3}) and specific heat capacity (J· kg^{-1}·℃$^{-1}$), respectively and the subscript of w represents the water. This equation neglects a dispersion term. U_{cv_h} and U_{cd_h} in HS unit are calculated by follows:

$$U_{cv\_h} = \rho_W c_w (T_p P_{h\_a} + T_{pas} P_{h\_pas} - T_h ET_h - T_h Q_{h-s} - T_h Q_{h-f} + T_{pas} V_{pas\_in} - T_h V_{pas\_in})$$

$$\tag{5}$$

$$U_{cd\_h} = k_w \frac{T_r - T_h}{\epsilon_h} S_h \times 3600 \tag{6}$$

where T represents the temperature (℃) and the subscripts of p and r represent rain water and rock, respectively; the subscripts of a and pas represent the active and passive stores in HS unit, and V_{pas_in} is water volume from the active store to the passive store (m³); P_{h_a} and P_{h_pas} represent the rainfall infiltration into the active and passive stores (m³), respectively, and which can be calculated by an exponential equation with the constants of α and β in Table 2 (Zhang et al., 2019); S_h represents cross area of heat flux (m²), which can be estimated by $V_h = S_h \bullet 2\epsilon_h$ based on the assumed equivalent distance and cubic geometry in this model (Fig. 4); ϵ_h represents the equivalent distance between two substances through which heat conduction occurs (m) (the two substances here are water and rock); k represents thermal conductivity (W·m^{-1}·℃$^{-1}$). Multiplying 3600 on the right side of Eq. (6) is to estimate the hourly heat fluxes. In many other heat models (e.g., Becker et al., 2004), groundwater temperature is often assigned a specific constant value (e. g. mean annual air temperature). In this model, the water temperature T_{pas} in the passive store is assumed to equal rock temperature as $T_{pas} = T_r$.

In depression, the heat transport along fast and slow flow paths can be expressed similarly. The heat transport in the slow flow reservoir is calculated as:
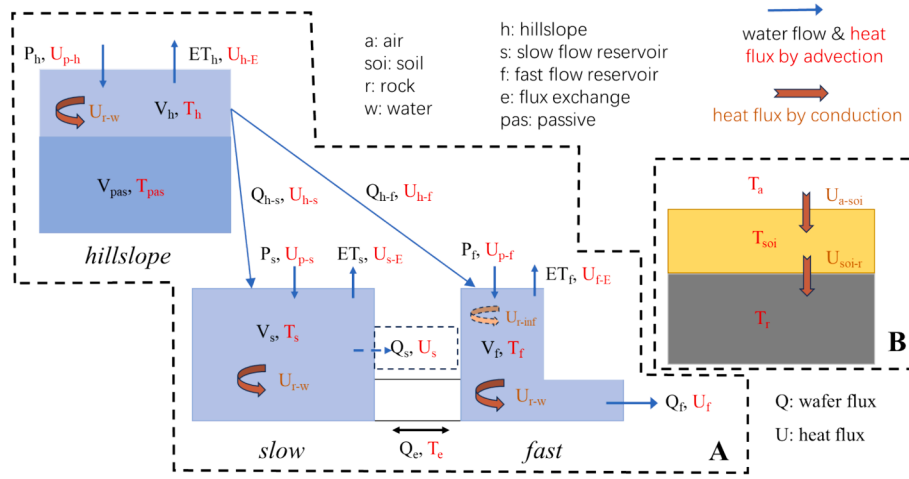
Fig. 3. Structure of the coupled water-heat model based on the conceptual model framework by Zhang et al. (2019). Schematic A represents the water flows, heat flows leaded by advection (red), and conduction from rock to water (orange); Schematic B represents the heat flows from air to soil and soil to rock by conduction (orange), respectively. The letter T in each reservoir in schematic A represents water temperature, which in schematic B represents medium (soil or rock) temperature. (For interpretation of the references to colour in this figure legend, the reader is referred to the web version of this article.)

Table 2
Description of model parameters, ranges and means derived from the best 500 parameter sets after calibration.

Subroutine	Parameters	Initial range 1	Initial range 2	Calibrated range	Mean	Descriptions
Flow routing	K_s (h)	20–500	25–350	41–199	90	The slow flow reservoir constant
	K_f (h)	1–100	1–90	8–26	14	The fast flow reservoir constant
	K_e (h)	300–7000	490–5500	490–5100	1945	Exchange constant between the two reservoirs
	f (−)	0.001–0.1	0.001–0.08	0.005–0.049	0.02	The ratio of porosity of the quick to slow flow reservoir
	a (−)	0.5–1	0.5–1	0.5–0.98	0.72	Precipitation recharge coefficient for slow flow reservoir
	w (−)	0.001–0.05	0.001–0.04	0.001–0.02	0.01	The hillslope unit constant
	b (−)	0–1	0.05–0.9	0.3–0.86	0.47	Recharge coefficient of hillslope to slow flow reservoir
Heat transfer	α (−)	5000–20000	5020–20000	5035–19983	12,277	Constant for calculation of rainfall recharge into the active store in hillslope
	β (−)	0–1	0.001–1	0.002–1	0.48	
	φ (−)	0–1	0.001–0.99	0.004–0.99	0.49	Coefficient for exchange flow between active and passive stores in hillslope
	ε_{inf} (m)	0.01–0.2	0.01–0.13	0.01–0.1	0.04	Equivalent distance between infiltration water and rock in fast flow reservoir
	ε_h (m)	0.01–1.5	0.01–1.1	0.01–1	0.5	Equivalent distance between water and rock in hillslope
	ε_f (m)	0.01–2	0.03–2	0.09–2	1.04	Equivalent distance between water and rock in fast flow reservoir
	ε_s (m)	0.01–8	0.01–5	0.01–4.2	1.06	Equivalent distance between water and rock in slow flow reservoir
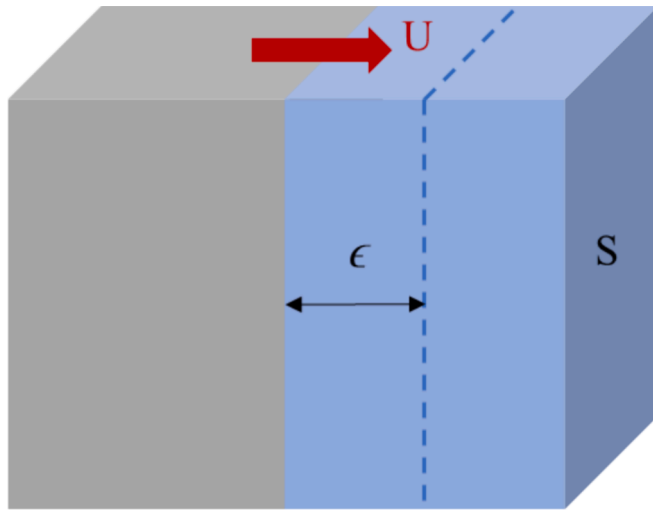
Fig. 4. Schematic illustration of heat conduction exchange for cubic geometry. Note: ϵ represents the equivalent distance between two substances through which heat conduction occurs (m), and S represents cross area of heat flux (m^2).

$$\frac{d\rho_W c_w (T_s V_s)}{dt} = U_{cv\_s} + U_{cd\_s} \tag{7}$$

$$U_{cv\_s} = \rho_W c_w (T_p P_s - T_s ET_s + T_h Q_{h-s} - T_s Q_e) \tag{8}$$

$$U_{cd\_s} = k_w \frac{T_r - T_s}{\epsilon_s} S_s \times 3600 \tag{9}$$

The heat transport in the fast flow reservoir is calculated as:

$$\frac{d\rho_W c_w (T_f V_f)}{dt} = U_{cv\_f} + U_{cd\_f} \tag{10}$$

$$U_{cv\_f} = \rho_W c_w (T_{inf} P_f - T_f ET_f + T_h Q_{h-f} + T_s Q_e - T_f Q_f) \tag{11}$$

$$U_{cd\_f} = k_w \frac{T_r - T_f}{\epsilon_f} S_f \times 3600 \tag{12}$$

where T_{inf} is the infiltration flow temperature of the fast flow reservoir. Since infiltration water T_p of the fast flow reservoir passes rock fractures and thus there is a conductive heat from rock. T_{inf} is estimated as:

$$T_{inf} = T_p + (k_w \frac{T_r - T_p}{\epsilon_{inf}} S_{inf} \times 3600) / (\rho_W c_w) \tag{13}$$

where the subscript of *inf* represents infiltration.

The above equations contain variations of rock temperatures (T_r) affected by heat conduction from soil, which can be calculated by:

$$\frac{d\rho_r c_r(T_r V_r)}{dt} = U_{soi\_r} \tag{14}$$

$$U_{soi\_r} = k_r \frac{T_{soi} - T_r}{\epsilon_r} S_r \times 3600 \tag{15}$$

Similar as rock, soil temperature T_{soi} can be calculated by:

$$\frac{d\rho_{soi} c_{soi}(T_{soi} V_{soi})}{dt} = U_{air-soi} \tag{16}$$

$$U_{air-soi} = k_{soi} \frac{T_{air} - T_{soi}}{\epsilon_{soi}} S_{soi} \times 3600 \tag{17}$$

where the subscript of *soi* and *air* represent soil and air; U_{air_soi} and U_{soi_r} represent the conductive heat fluxes from air to soil and from soil to rock, respectively; V_{soi} and V_r represent the volumes of soil and rock (m^3) in the shape of cuboids (Fig. 4), respectively. The equivalent distances of soil layer (ϵ_r) are equal to 0.3 m and 1 m for HS and depression units, according to the soil thickness distribution. The equivalent distance of ϵ_r is equal to the mean thickness of the epikarst in this catchment (10 m).

Typically, the karst fracture rate is relatively low (e.g., approximately 10 % according to field investigations of rock fractures in this catchment). Therefore, the model solely includes the heat conduction from rock to water and neglects the heat conduction from water to rock.

3.1.3. Water age estimation

Water ages are simulated in the HS unit (containing active and passive reservoirs) using the partial mixing method:

$$\frac{dA_h(V_h)}{dt} = A_p P_{h\_a} + A_{pas} P_{h\_pas} - A_h ET_h - A_h Q_{h-s} - A_h Q_{h-f} \\ + A_{pas} V_{pas\_in} - A_h V_{pas\_in} \tag{18}$$

$$\frac{dA_{pas}(V_{pas})}{dt} = A_p P_{h\_pas} - A_{pas} P_{h\_pas} + A_h V_{pas\_in} - A_{pas} V_{pas\_in} \tag{19}$$

where *A* represents water age.

Water ages are estimated in the fast and slow flow reservoirs in depression as:

$$\frac{dA_s(V_s)}{dt} = A_p P_s - A_s ET_s + A_h Q_{h-s} - A_s Q_e \tag{20}$$

$$\frac{dA_f(V_f)}{dt} = A_p P_f - A_f ET_f + A_h Q_{h-f} + A_s Q_e - A_f Q_f \tag{21}$$

The model used in this study considers the "aging effect", as each age item at time *t* includes the age at the previous time step *t-1* in the calculation.

The model comprises 14 parameters that require calibration, 7 for flow routing (K_s, K_f, K_e, f, a, w and b) and 7 for water temperature calculation (α, β, φ, ε_{inf}, ε_h, ε_f and ε_s). The descriptions of model parameters for calibration are listed in Table 2.

3.2. Modelling procedure

The model inputs include meteorological variables of precipitation and air temperature as well as the rainwater temperature. Here, the rainwater temperature is equal to air temperature minus mean difference between air temperature and rainwater temperature in this area (1.1 ℃). The calibration period was from November 1, 2016 to October 31, 2018, and the validation period was from November 1, 2018 to October 31, 2019. To minimize the effects of initial conditions on water age calculations, data from three months prior to calibration (from 23 July 2016 to 31 October 2016) were used as a spin-up period. The modelling was implemented at hourly time steps.

The modified Kling-Gupta efficiency (KGE) criterion (Kling et al.,

2012) was utilized as the objective function for model calibration and validation. Model parameters were jointly calibrated based on observed series of discharge and water temperature at the catchment outlet, using the combined criterion of KGE as: KGE = (KGE$_d$ + KGE$_T$)/2, where KGE$_d$ was for discharge and KGE$_T$ was for water temperature. The measured data of soil temperatures at depths of 20 cm and 40 cm, as well as the water temperatures at the HS spring and wells in the depression, were also used to evaluate the performance of the model. A Monte Carlo method was employed to calibrate the model parameters and assess the model's effectiveness. The parameter calibration process consisted of two iterations. Firstly, within the initial given ranges of parameters (initial range 1 in Table 2), 100,000 sets of parameter combinations were randomly generated according to a uniform distribution. The ranges were then narrowed down using the criterion of KGE>0.3. Then, another random sampling was carried out using the narrowed ranges of parameters (initial range 2 in Table 2), generating another 100,000 sets of parameters. The best (in terms of the efficiency statistics) parameter populations of 500 sets of parameters corresponding to the highest KGE values of the simulated results were selected for model evaluation and result analysis.

According to previous field survey in this catchment (Zhang et al., 2011) and literature values (Fan, 2003; Wang, 2008), some parameters were fixed. Hence, the density (ρ) of water, soil and rock were 1000, 1200 and 2600 kg m^{-3}, respectively. The specific heat capacity (*c*) of water, soil and rock were 4200, 2400 and 680 J· kg^{-1}·℃$^{-1}$, respectively (Song et al., 2019; Wang et al., 2019). The thermal conductivity (*k*) of water, soil and rock were 0.48, 1.9 and 2.5 W·m^{-1}·℃$^{-1}$, respectively (Duan, 2015; Song et al., 2019). All other parameters were calibrated.

4. Results

4.1. The simulated flow and temperature

The results showed that the measured discharge and water temperature over the study period were mostly bracketed by the simulation ranges for the 500 best parameter populations at the catchment outlet (Fig. 5). The average KGE values were 0.72 (with a range from 0.63 to 0.77) and 0.73 (0.63 to 0.85) for calibrated and validated periods, respectively. With this parameter sets, the average KGE$_q$ values were 0.76 (0.58 to 0.83) and 0.75 (0.64 to 0.83), and the average KGE$_T$ values were 0.69 (0.56 to 0.76) and 0.71 (0.51 to 0.89), respectively. The simulated dynamics of flow and water temperature at the catchment outlet (the underground conduit flow) can generally capture the respective variable variations in response to seasonal temperature variability and rainfall events. However, some flood peaks, especially in 2018, were underestimated (Fig. 5a), and the simulated temperature exhibited more pronounced fluctuations compared to the observed values (Fig. 5b).

The modelled soil temperature at 20 and 40 cm, calculated according to Eq.16 and 17 (the equivalent distances of soil layer, ϵ_{soi} were set to 0.2 and 0.4 m, respectively), are shown in Fig. 6. The results demonstrated that the model effectively captured the variations in soil temperature at the depths of 20 cm and 40 cm, with KGE$_{ST}$ for soil temperature of 0.72 and 0.63, respectively, during the study period.

The observed water temperatures at HS spring and depression wells represented observations at specific points, instead of the whole HS unit and slow flow reservoir in the depression. Hence, in this study, the comparison between simulated and observed water temperature changes at HS spring and the groundwater wells were regarded as "soft verification". The results showed that the seasonal variation of simulated water temperature at the HS spring was consistent with that of observation at the whole HS unit (Fig. 7(a)). Building on the findings of previous Electrical Resistivity Tomography (ERT) surveys, the limestone stratum overlying the aquitard, a thin marlstone layer, on the HS where monitoring site S5 is situated, is subject to intense weathering, resulting in the formation of well-developed karstic fractures (Cheng et al., 2019).
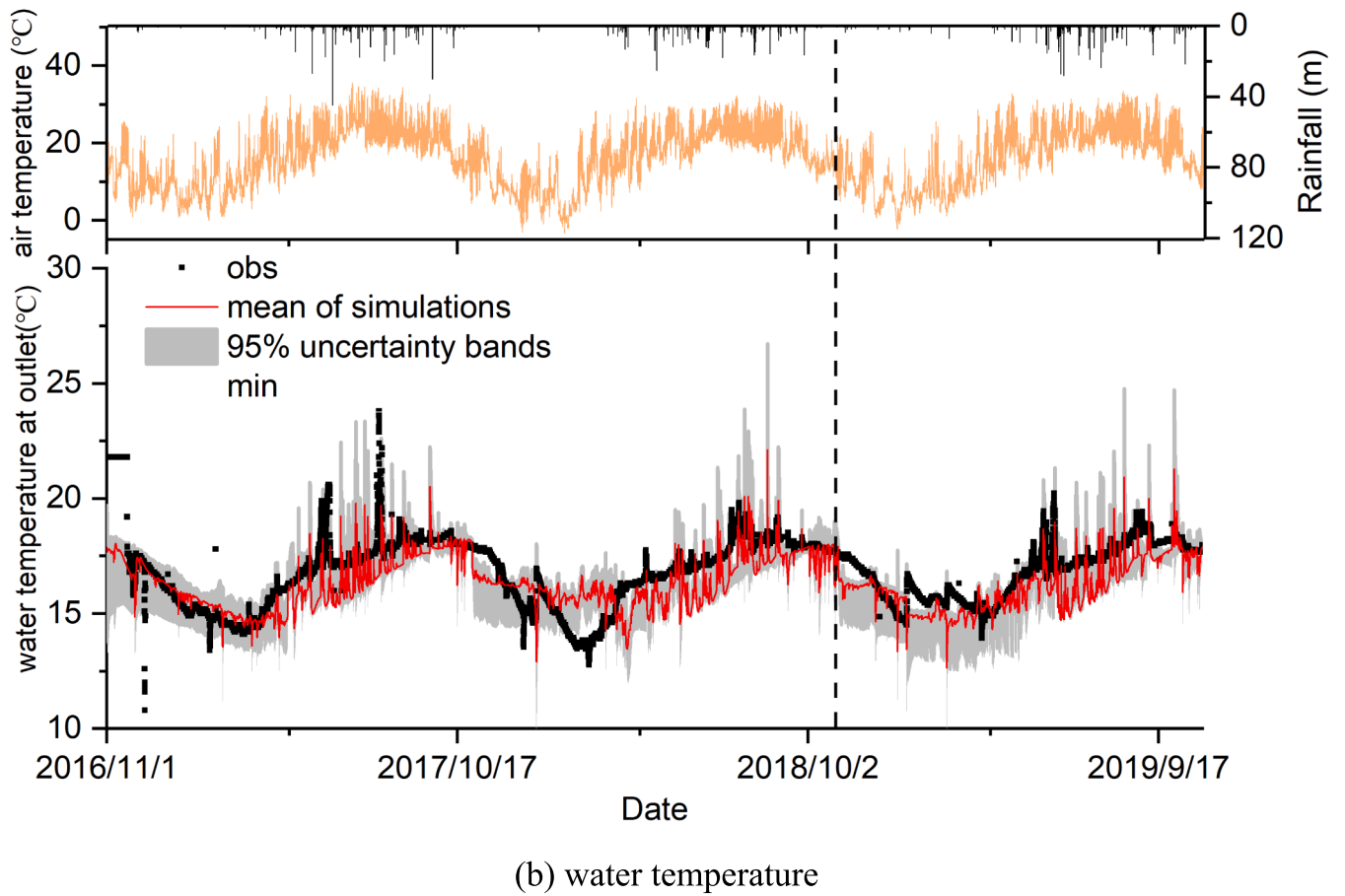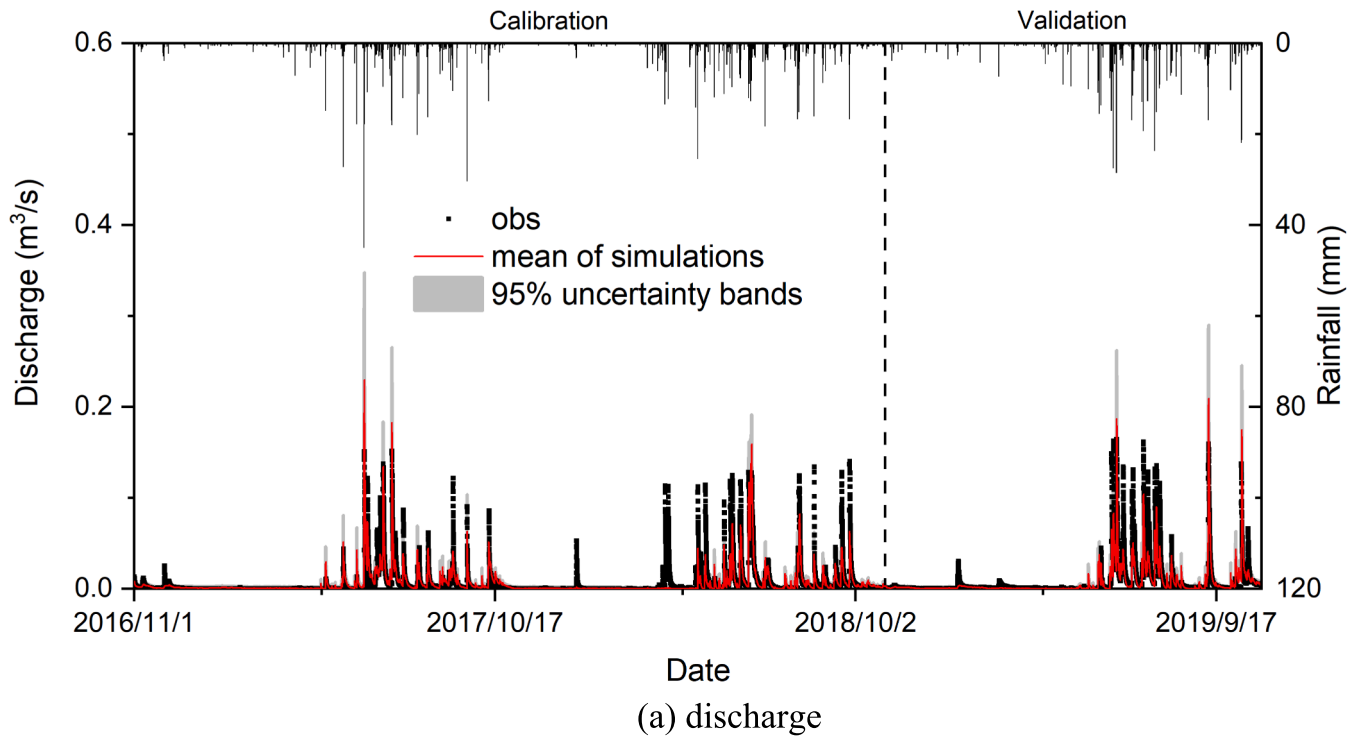
(a) discharge

(b) water temperature

Fig. 5. Simulated and observed flow and water temperature at the catchment outlet over the study period.
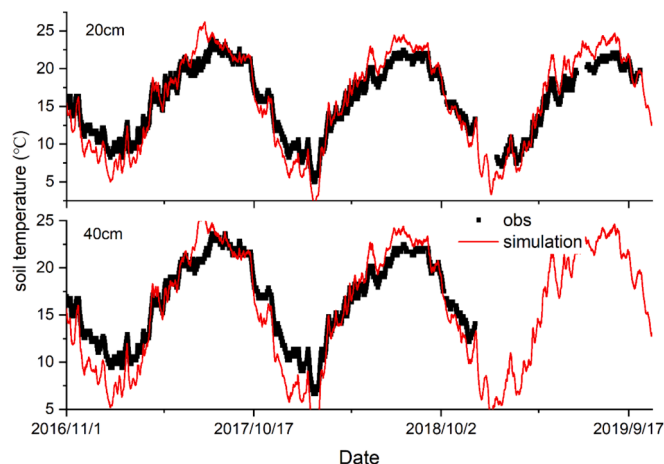
Fig. 6. Simulated and observed soil temperatures at 20 and 40 cm depth over the study period.

Consequently, the retention capacity of this HS is limited, leading to a rapid hydrological response at S5 following precipitation events (Zhang et al., 2020c). This dynamic may contribute to relatively swift fluctuations in spring temperatures at this location. In contrast, the model-simulated temperatures are indicative of the average conditions within the catchment's HS unit. Thus, compared to S5, the modelled temperature graph of the HS unit exhibits a more gradual response with smaller amplitude fluctuations. Nevertheless, the correspondence in overall trends provides indirect validation of the model's performance.

In the depression unit, the model's representation of the slow flow reservoir accurately reflects the gentle variations of water temperatures observed at the four depression wells (Fig. 7b). However, replicating some exceptionally high temperature readings in wells 1# and 3#, which are interconnected with extensive lateral fractures, presents a challenge (Fig. 7b). Notably, the model is adept at capturing the attenuation of water temperature fluctuations at well W5, where the conditions suggest a less permeable aquifer containing "older" groundwater

(Chen et al., 2018).

The mean values of calibrated model parameters were listed in Table 2. The probability density of each parameter was estimated for the 500 best parameter populations after calibration, as shown in Fig. 8. The results indicated that among the parameters related to flow routing, k_s and k_f were the most sensitive and identifiable parameters, with values concentrated in the range of 40–80 h and 10–20 h, respectively. Parameters a, f and b were relatively sensitive, with values concentrated in the range of 0.7–0.8, 0.01–0.03 and 0.3–0.6, respectively. The parameters K_e and w were insensitive. Among the parameters related to temperature calculations, only ε_{inf} and ε_s were sensitive parameters, with values concentrated in the range of 0.01–0.03 and 0.1–1, respectively, while the remaining parameters (α, β, φ, ε_h, and ε_f) were poorly identified.

4.2. Simulated water age distributions

The simulated flux ages in various reservoirs over the study period are shown in Fig. 9. The average flux age at the catchment outlet (the fast flow reservoir) during the study period was 260 days, exhibiting significant seasonal and daily variations, especially during the wet season. The flux ages could reduce from around 500 days before rainfall to less than 10 days after a storm event (Fig. 9(a)). Compared to the catchment outlet, the water ages in the HS unit were generally lower, with an average value of 80 days (with maximum and minimum values of 168 and 16 days, respectively) during the study period. The water ages within the slow flow reservoir (i.e. matrix and fine fractures) remained at a relatively high level, with an average value of 452 days (with maximum and minimum values of 510 and 380 days, respectively) during the study period. From the results, flux ages at the slow flow reservoir approach those at the catchment outlet during the dry season (Fig. 9a), which indicated that the catchment outflow was primarily fed by the water in matrix and small fractures. Conversely, flux ages at the HS unit approach those at the catchment outlet during the wet season, which signifies a significant contribution of the hillslope to the catchment outflow under wet conditions. Furthermore, during heavy rainfall events, the water ages of the catchment outflow could be as short as a few days, shorter than that in the HS unit. It infers an additional
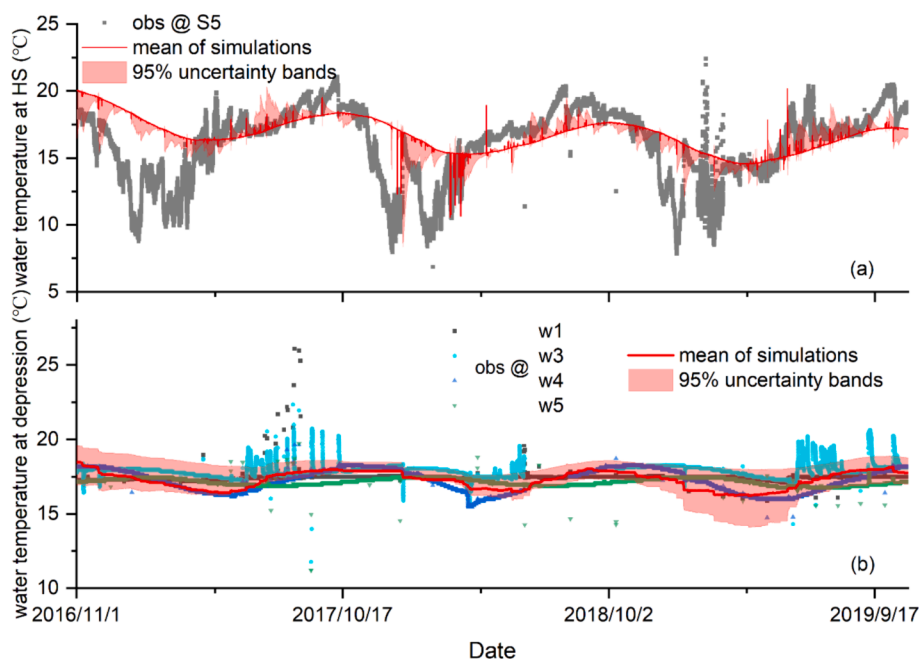

Fig. 7. Simulated and observed water temperature at HS (a) and depression units (b) over the study period. Note: at the HS unit, the observed and simulated water temperature T_h represents T_h at a HS spring and the whole HS unit, respectively; at the depression unit, the observed and simulated water temperature T_s represents T_s at wells and the whole depression unit, respectively.
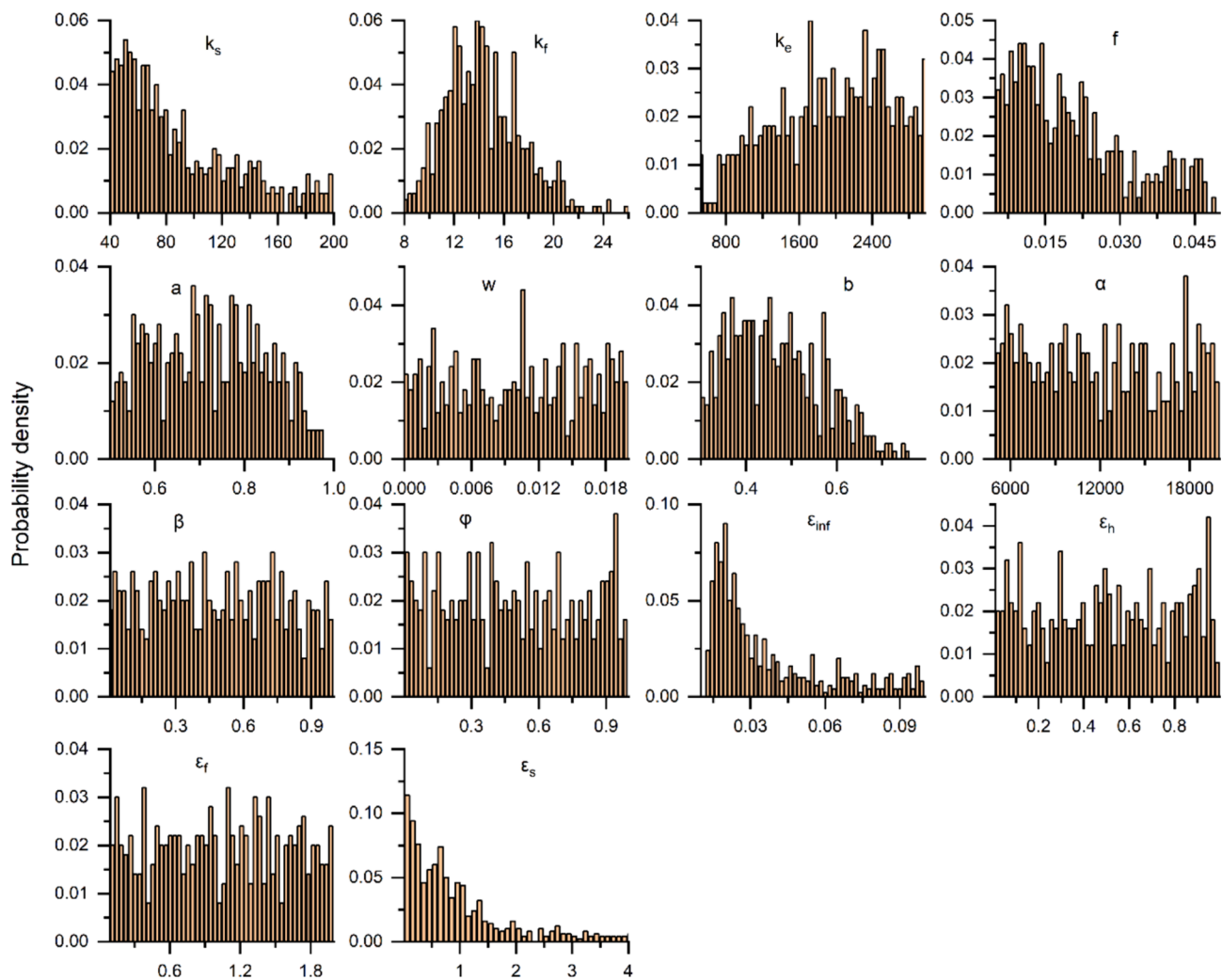
Fig. 8. Probability density estimate of the 500 best parameter populations.

contribution of water recharge to the outlet, such as the concentrated recharge through sinkholes and preferential flow pathways in the depression. These inferences were consistent with previous findings on the hydrological function of this karst catchment (Wang et al., 2020; Yue et al., 2020; Zhang et al., 2021b).

To better understand the dynamics of water age distributions under different wetness conditions, two time points in the wet and dry seasons were selected, respectively, for the tracking analysis. The wet season time point (t1) was chosen as June 12, 2017, with rainfall amount of 45 mm and a maximum discharge at the catchment outlet of 0.15 m^3/s on this day. The dry season time point (t2) was selected as March 14, 2018, with rainfall amount of 5.4 mm and a maximum discharge at the catchment outlet of 2.5 × 10^{-4} m^3/s on this day. Fig. 9(b) showed the average probability density function (PDF) of flux age at the catchment outlet simulated using the tracer of temperature at t1 and t2. The results indicated that, for the two time points, about 68 % and 37 % of the catchment outflow came from the contribution of rainfall recharge on the corresponding day (t1 and t2), respectively. Although the catchment outlet continuously received water from previous rainfall in a long term, these contributions were significantly lower (e.g. the contribution of rainfall from previous individual events is less than 10 % for t1 and t2) than the same-day rainfall inputs (Fig. 9b). The transit time PDFs with other wetness conditions had similar variation patterns (Fig. S1 (a) in the Supplement). This indicated that, on rainy day, the fresh water (rainfall recharge) was the primary source contributing to the catchment outflow rather than the old water stored in the aquifer.

The simulated transit time distributions (TTD) were shown in Fig. 10. The average transit time PDF exhibited relatively high fractions of young water with low transit times (e.g. less than 50 days) (Fig. 10(a)), which highlighted the contribution of flow through fast pathways to the outflow in the Chenqi karst catchment. The cumulative probability density function (CDF) of transit times showed that young water with low transit times accounted for less than 30 %, which indicated that a notable portion of rain water was either stored in the aquifer or consumed through evapotranspiration, rather than draining as runoff from the catchment outlet. The simulated TTD for events with different wetness conditions were represented in Fig. 10(b), which showed that the transit time PDFs had similar variation patterns for rainfall at t1 and t2. However, according to the simulated transit time CDF, compared to the wet season, a higher portion of rain water remained in the aquifer, with less draining as runoff from the catchment after precipitation in dry season. This can be supported by the variation patterns of TTD under different wetness conditions (Fig. S1 (b) in the Supplement).
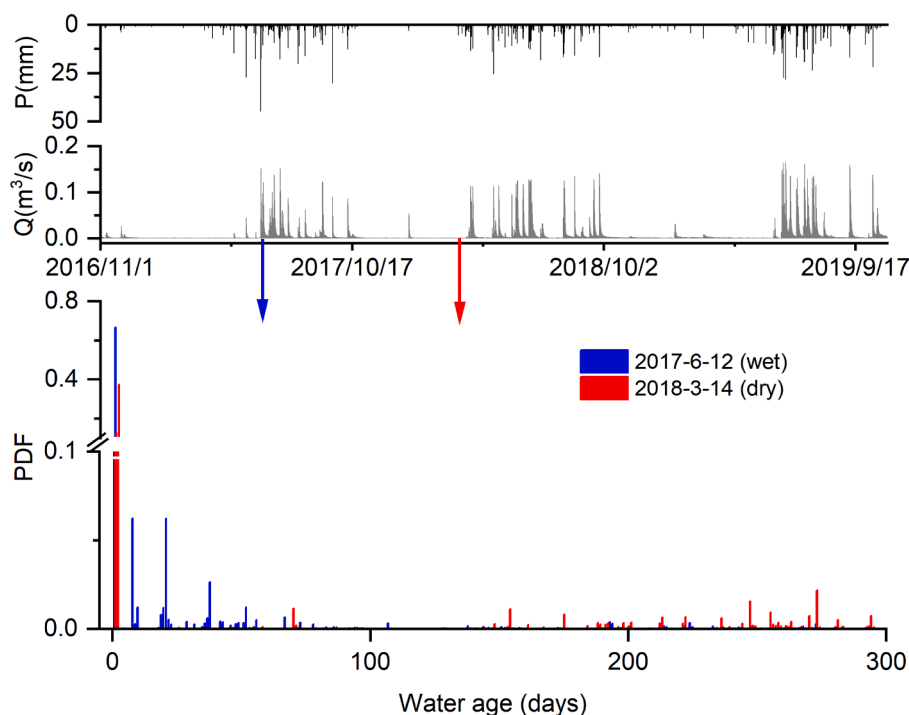
5. Discussion

5.1. Simulating water temperature in karst catchments using a conceptual model

The skill of a coupled flow-tracer model to accurately simulate the dynamics of a tracer flux in a catchment is the basis for tracking water age distributions, as well as the fundamental demonstration of
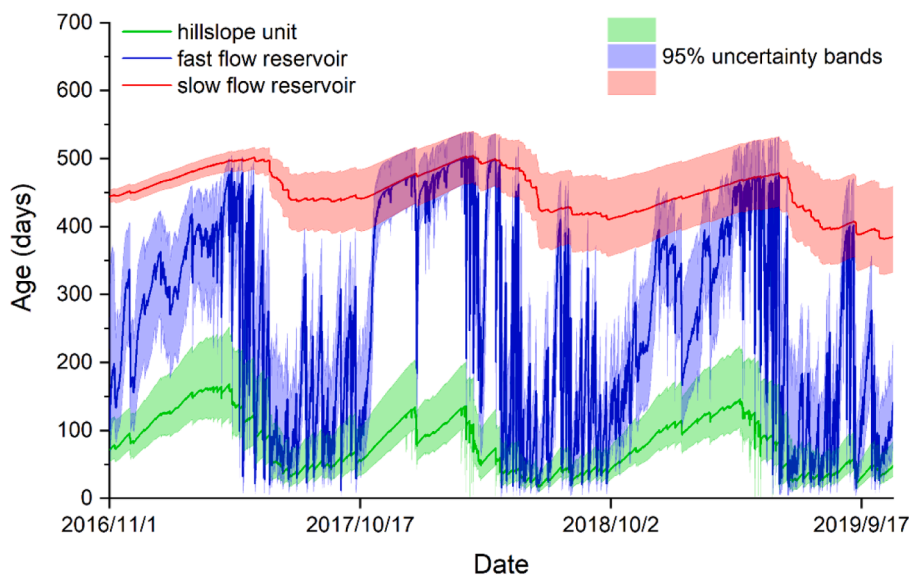
(a) mean flux ages

(b) flux age distribution

Fig. 9. Simulated (a) mean flux ages in various conceptual reservoirs (for the 500 best parameter populations), and (b) flux age distributions at the catchment outlet at t1 and t2 (for the best parameter set).

minimizing the impact of non-conservative behaviour at the catchment scale. Although the simulation of the water flow-temperature process in a catchment has been achieved in some studies through physically-based models (Zhang et al., 2000; Qiu et al., 2019), it is still difficult to apply to the simulation of water temperatures in karst catchments. Especially for the dynamic simulation of water temperature in fissure or conduit flows, numerical experiments or calculations of water temperature in single fissure or conduit are still predominant (Covington et al., 2011, 2012; Luo et al., 2023). Existing studies have demonstrated that conceptual models were able to simulate the spatial and temporal dynamics of

tracers in different landscape units of karst catchments, such as stable isotopes of hydrogen and oxygen (Zhang et al., 2019; Li et al., 2022). The availability of long-term soil temperature, water temperature at HS spring and depression wells in the Chenqi catchment provided the foundation for testing the use of conceptual models to simulate spatio-temporal variations in water temperature in karst catchments.

Adapting the tracer-aided conceptual model of Zhang et al (2019) using temperature as a tracer allowed the variations in water temperature in different landscape units to be simulated to a first approximation. At the catchment scale, such models enable the complex dynamics of
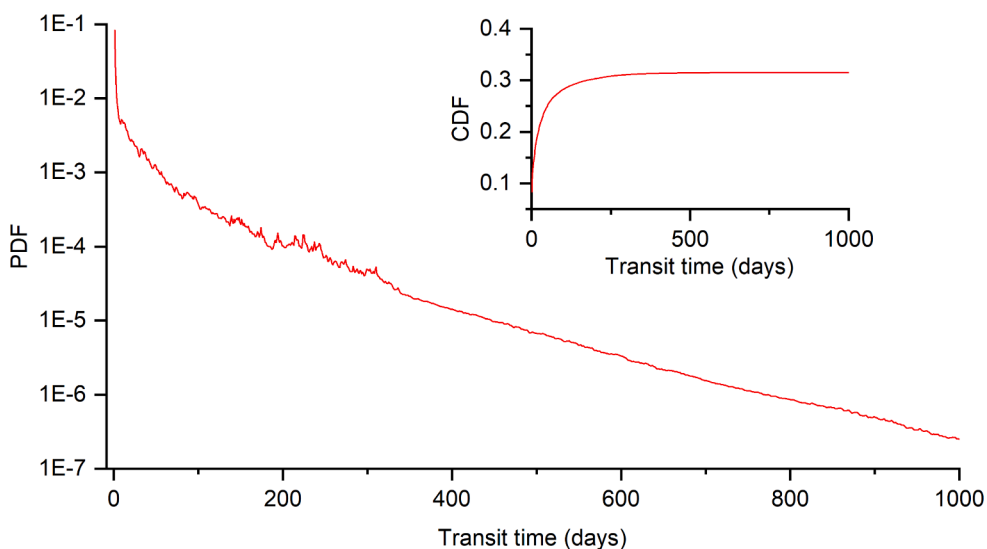
(a) mean of transit time distribution (PDF and CDF)
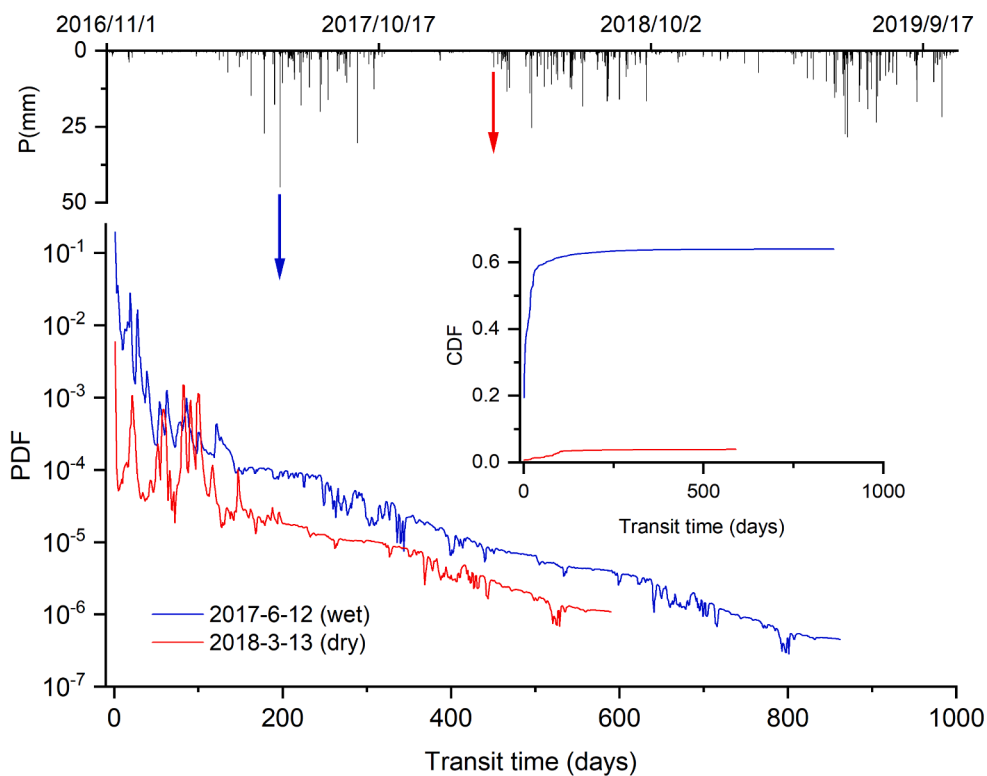
(b) transit time distribution under different wetness conditions (PDF and CDF)

Fig. 10. Transit time distributions simulated by the tracer-aided model using the best parameter set, (a) the mean TTD during the study period, (b) TTD for the rainfall at t1 and t2.

water flow and heat fluxes in karst regions to be simulated using conceptual models with simple structures and fewer parameters. Despite the use of a simple tank structure and simplified heat transfer calculations in the model (such as the use of 'equivalent distance' to estimate conduction between water flow and the mediums of soil and rock (as shown in Fig. 4), while calibrating parameters using outflow temperature at the outlet, the model simultaneously improved the accuracy of simulating water temperature dynamics by "soft validation" using water temperature in HS spring flow and groundwater wells, as well as soil

temperature at different depths. Such an approach has been adopted in other studies, which found that checking against soft data can reveal incompatibilities between data and calibration (Wu et al., 2023).

In many water-heat transport models, it is a common practice to calculate stream inflow temperature based on empirical relationships with air temperature or soil temperature (Haag and Luce, 2008; Ouellet et al., 2014; Morales-Marín et al., 2019). However, a core function of tracer-aided models is to estimate water age distributions at the catchment scale, which also requires the model to simulate different water

mixing processes in different landscape units. Hence, physically-based models have the parameters to directly represent storage and mixing in various landscape units inferred by temperature damping potentially have such tracking function (Zhang et al., 2000; Kwon and Koo, 2017; Sjöberg et al., 2021). Although the model in this study is conceptual, rather than fully physically-based, the method used to calculate inflow temperature considers the processes of heat advection and conduction. This is consistent with the requirement of tracer-aided model for tracking rainfall-flow processes at the catchment scale. Of course, the model still has some obvious limitations. For example, due to the shallow soil layer in karst areas, water flows in the fractures within the epikarst are the main source of underground conduit runoff (Williams, 2008; Fu et al., 2016), and their temperatures play a controlling role in the underground conduit inflow temperature. However, it is difficult to observe the temperature of rock in such heterogeneous systems, which leads to inadequate constraints on the parameter calibration for the model's calculation of heat conduction between fracture water and rock, thereby affecting the accuracy of the temperature simulations. Nonetheless, the model established in this study provided a reasonable representation of water flow and seasonal heat transfer processes in the karst hydrogeological system. It also adhered to the relatively parsimonious philosophical basis of catchment process simulation, representing an encouraging step forward in water temperature modeling in karst catchments.

Compared to the observed sequences, the simulated hourly temperatures in the catchment outflow exhibited significant fluctuations, particularly after rainfall in the wet season (see Fig. 5b). This phenomenon also frequently occurred in other studies (Yearsley et al., 2019). The most likely reason for this was an overestimation of the contribution of rainfall infiltration (young water) to the underground conduit flow. It can be inferred that the calibrated parameters for the conceptualization of the preference for releasing younger and older water from the karst hydrogeological system, linked to the "inverse storage effect" and "direct storage effect" (Harman, 2015; Wilusz et al., 2020), could be inaccurate. In this model, the parameters for calculation of water flux between different reservoirs are fixed (such as parameter *b* in Table 2), without considering the enhanced connectivity resulting from increased water storage which could significantly increase the catchment outflow during heavy rainfall events (Zhang et al., 2021b), which is consistent with the underestimates of discharge peak in Fig. 5(a). This further causes the model parameters to take on values that tend to increase the "inverse storage effect" of catchment, although it may be inaccurate under drought conditions. However, on the other hand, this precisely demonstrated the significant indicative role of temperature for different water sources (as shown in the simulated results in Fig. 7), which has been confirmed in many studies that use temperature information to separate runoff components in karst catchments (Genthon et al., 2005;

Domínguez-Villar et al., 2018; Chi et al., 2020), laying the foundation for its potential transfer value as an inexpensive and logistically simple tracer to build tracer-aided models and simulate water age distributions in other karst catchments.

5.2. Comparisons of water age distributions modelled using tracers of stable isotopes and water temperature

In previous studies, the use of stable isotopes in a tracer-aided runoff model has proven effective in tracking the water age distributions in the Chenqi catchment (Zhang et al., 2019, 2020b). The simulated flux ages in the underground conduit and HS units using temperature in this study were very similar to those simulated using isotopes during the study period (Fig. 11a and c). In contrast, there were notable differences between the flux ages in the slow flow reservoir simulated using temperature and isotopes (Fig. 11b). Many studies based on isotope-based tracer-aided models have shown that the mixing volume for slow flow reservoir is usually poorly identifiable, which leads an uncertainty of the slow flow ages (Soulsby et al., 2015; Zhang et al., 2019; Gou et al., 2023). Furthermore, apart from this reason, the uncertainty in the flux ages in the slow flow reservoir using temperature as a tracer might also be related to inaccuracies in the temperature simulation. The large contact area between water and the slow flow media combined with the long water residence times (Husic et al., 2019; Zhang et al., 2021b) result in heat conduction having a significant impact on water temperature in the slow flow reservoir. In this study, we simplified the calculation of heat conduction between medium-water, medium-medium, and within the medium, which may affect the accuracy of simulating the flux ages in slow flow reservoir. Hence, regardless of whether isotopes or temperature was used as a tracer for model constraints, there was notable uncertainty in the simulation results of flux ages in slow flow reservoir.

For the best 500 runs, the probability density functions (PDFs) of simulated flux ages at the catchment outlet exhibited two distinct peaks (Fig. 12c), one for younger water and the other for older water, reflecting the contributions of flows from the HS unit and slow flow reservoir to the outlet under different wetness conditions. This pattern was consistent with that modeled using the tracer of isotope by Zhang et al., (2019). However, higher proportions of waters with youngest ages (such as younger than 50 days) and oldest ages (such as older than 450 days) were evident in the PDFs of simulated flux ages at the catchment outlet derived using temperature (Fig. 12c). The flux age PDFs in HS unit simulated using temperature and isotopes were similar (Fig. 12a). Hence, it could be deduced that, for the first peak in water age PDFs of catchment outflow (in Fig. 12c), the difference in the proportion of extremely young water in the outflow simulated using temperature and isotopes may be primarily caused by capturing the direct infiltration of
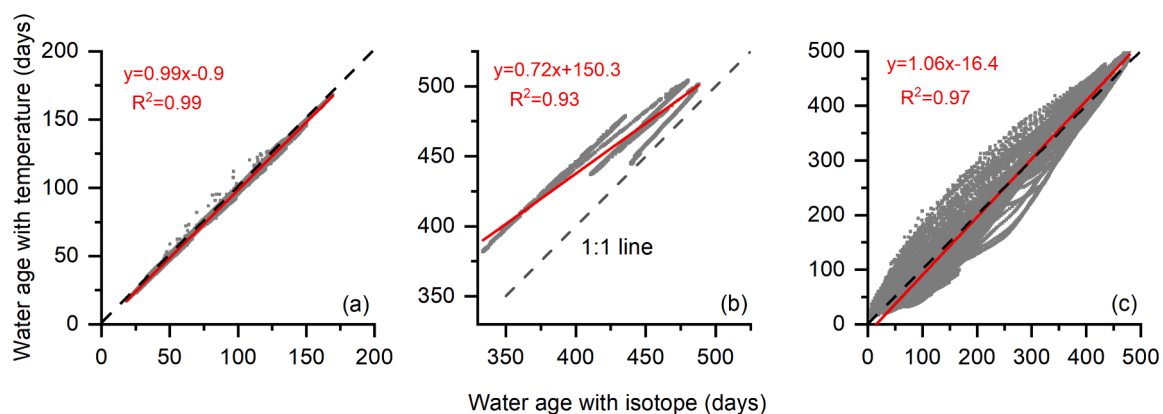

Fig. 11. Simulated water ages of fluxes in different conceptual stores using temperature and isotope, respectively, (a) HS unit, (b) slow flow reservoir, and (c) fast reservoir (the catchment outflow).
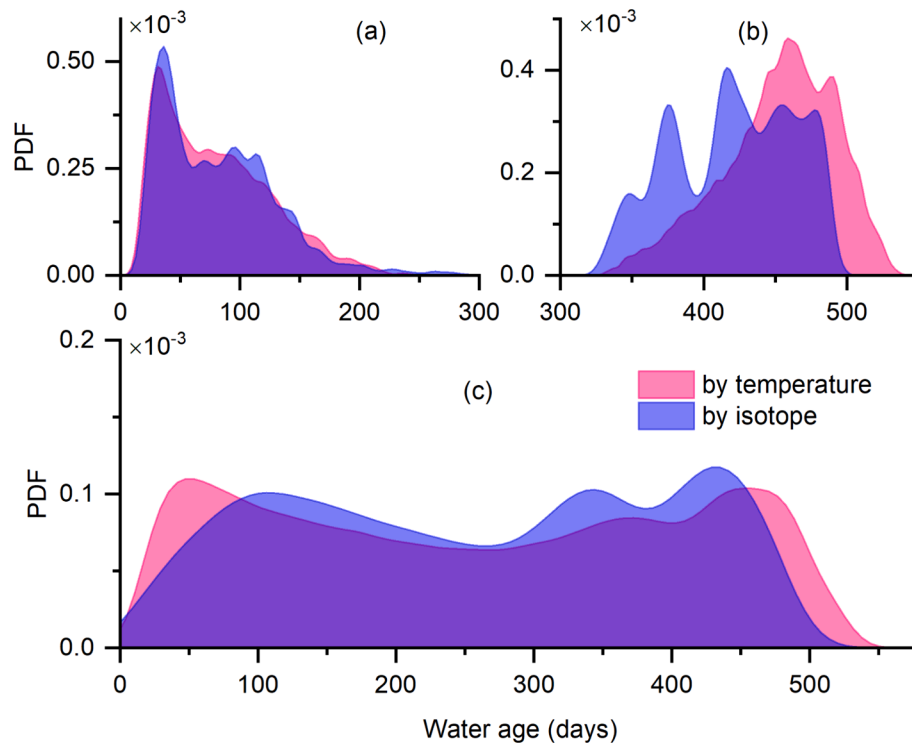
Fig. 12. Probability density functions of the simulated water ages in fluxes from (a) HS unit, (b) slow flow reservoir, and (c) fast reservoir for the best 500 runs, using temperature and isotope, respectively.

new water through sinkholes or exposed large fractures during heavy rainfall events. The isotopes in directly infiltrated water experience less fractionation during the percolation process (Sprenger et al., 2017), leading to a notable difference in its isotopic composition compared to the older water stored in underground conduits (Chen et al., 2018). In contrast, directly infiltrated water was influenced by heat conduction with contact media, resulting in rapid changes in its temperature, which may reduce differences in the temperature with the older water in underground conduits (Luo et al., 2023). Therefore, using temperature as a tracer may tend to overestimate the proportion of new water in the outflows in karst catchments.

On the other hand, for the second peak in water age PDFs of catchment outflow (in Fig. 12c), the higher proportion of older water in the outflow simulated using temperature than that simulated using isotopes was mainly caused by variations in the flux age distribution in the slow flow reservoir (Fig. 12b). For isotopes, the evaporative fractionation in mobile waters is weak (Sprenger et al., 2018), which leads significant differences in isotope composition in waters with different ages, namely, isotopes have a strong "fingerprint" effect in the conceptual store. In contrast, the temperature of water in the slow flow reservoir is influenced by heat conduction, which causes the temperature of waters with different ages to tend to be similar (Brookfield et al., 2017; Chen et al., 2018), leading to a weakening of the "fingerprint" effect. Therefore, compared to isotopes, the proportion of old water in the outflows simulated using the tracer of temperature could have a higher level of uncertainty.

The water transit time distributions simulated using temperature as a tracer constraint in Chenqi was overall quite comparable to those simulated using isotopes as a constraint (Fig. 13), indicating the applicability of temperature in water age distribution simulation in karstic catchments. The PDFs simulated using temperature decreased rapidly at the very short-tail of the distribution, i.e. < 10 d in Fig. 13, which suggests that the tracer-aided model using temperature can capture the dominant control of fast flow paths (e.g. the effects of sinkhole or large fractures) on the underground conduit flow generation early in rainfall
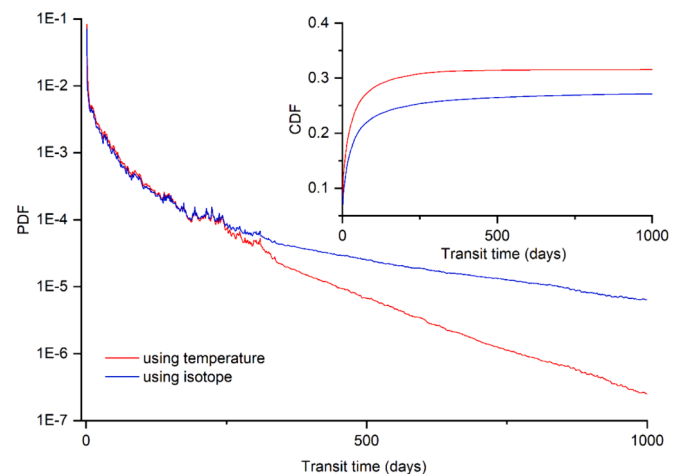

Fig. 13. Mean transit time distribution by the tracer-aided model with temperature and isotope, respectively.

events as well as models using isotope tracers. The transit time distribution simulated using temperature also captures the long tail of the distribution, albeit with a lower proportion of the flux, which inferring the influence of different older flow generating processes and associated mixing (Harman et al., 2009; Hrachowitz et al., 2013). It is worth noting that on average about 31 % of the precipitation entering during the study period was estimated using temperature to have left the catchment as stream flow within 3 years (the estimated CDF in Fig. 13), which revealed that there was a higher proportion of precipitation projected as being drained by fast flows from the results simulated using temperature. This was similar with the results simulated using isotopes, that about 27 % of the precipitation have left the catchment as stream flow within 3 years.

It can be seen that there were still be potentially influences of various

sources of uncertainty when using temperature as a tracer to simulate water age distributions in karst catchments. However, the overall conclusion of this study that a tracer-aided conceptual model constructed using temperature as a tracer can capture the dynamics of water ages in different landscape units remain largely unaffected.

5.3. Equifinality of model parameters and uncertainty of the modelled results

The application of a tracer-aided model that employs temperature as a proxy yields reasonable outcomes, yet it is hampered by substantial parameter equifinality and uncertainties in modelled outputs within intricate karst terrains. Parameter sensitivity analysis (see the in the Supplement), conducted separately for calibrations against outlet discharge and/or water temperature (quantified by indices such as KGE_d, KGE_t), underscores the issue of equifinality. Specifically, when calibration targets discharge alone, four parameters (K_s, K_f, α, and β) within the seven-parameter flow routing module emerge as sensitive, whereas temperature module parameters demonstrate insensitivity (seen in Fig.S2 (a) in the Supplement). Conversely, when calibration exclusively accounts for temperature, the flow routing module reveals K_f, K_e, f and α as sensitive, alongside ε_{inf} and ε_f within the temperature module as sensitive (Fig.S2 (b)). However, when calibrating against both discharge and temperature signatures, the flow routing module retains Ks, Kf, α, and β as sensitive, with ε_{inf} and ε_s in the temperature module showing sensitivity (Fig.S2 (c)). Notably, when optimizing for both discharge and temperature composition, parameters such as K_s, K_f, β, and ε_{inf} exhibit heightened sensitivity, surpassing those calibrated using temperature alone (as depicted by the broader cumulative distribution ranges in Fig.S2 (c)). By adopting a combined objective function, the two additional sensitive parameters (ε_{inf} and ε_s) in the temperature module complement the already sensitive quartet in the flow module (K_s, K_f, α, and β). Within this module, the three parameters of K_s, α, and β accentuate the 'old' water's contribution to outflow. In contrast, the fast flow reservoir constant (K_f) signifies the 'young' water's contribution to outflow. Augmenting K_s, α, and β or diminishing K_f engenders an increased release of older water from the slow reservoir to the catchment outlet. Inversely, parameter alterations in the opposite direction lead to younger outflows. The temperature module's parameters ε_{inf} and ε_s denote thermal diffusion from rocks to water permeating into the fast reservoir and the thermal characteristics of slow reservoir storage, thereby influencing water temperature at the outlet and the relative outflow contributions from both reservoir types. Although the dual-constrained calibration in this study utilizing discharge and temperature, parameter equifinality remains obvious, which might only be overcome when additional field data were used to better constrain parameters. Nonetheless, the utilization of temperature as a tracer proffers insights into storage dynamics, hydrologic connectivity, and mixing processes.

Although certain parameters (e.g., α, β, φ, ε_h, and ε_f, which govern fast flow reservoir and HS unit) are insensitive, the uncertainty bounds in modeled temperatures and ages are arrow (as seen in Figs. 7 and 9). This could be related to the calibration harnessing outlet data and the strong connectivity between HS unit and the catchment outlet. Whilst the broader uncertainty bands tend to arise in the slow flow reservoir, where mixing volumes often elude precise determination, as noted by other water age research at the catchment scale (Benettin et al., 2017; Li et al., 2022; Soulsby et al., 2015). According to flux age simulations (Fig. 9), uncertainty magnifies alongside flux ages within both HS unit and fast flow reservoirs. During the rainy season, with prominent HS contributions, outlet uncertainty diminishes; however, the slow flow system's dominance in the dry season inflates outlet uncertainty. Thus, the insensitive parameter K_e, which governs inter-reservoir exchange, could heighten uncertainties at both the slow flow reservoir and the catchment outlet.

Some flow peak underestimations in 2018 at the outlet possibly stem from calibration constraints driven by the prior year's significant events; extended calibration datasets might redress this. The model's misrepresentations of thermal fluctuations at the outlet signal a need for enhanced parameterization of heat transfer processes and flow mixing, which demand further examination.

For precise water age distribution predictions through this traceraided model, high spatiotemporal resolution data at the catchment scale prove crucial. Observation data across diverse wetness conditions—like intense rainfall events and extended dry spells which encapsulate hydrological connectivity and mixing propensities—are vital for simulation fidelity. Granular temperature measurements, encompassing those of soil, rock, rain, spring, groundwater, and outlet flows, afford a reduction in uncertainties related to heat diffusion and mixing process simulations. Fortunately, temperature's accessibility and affordability for tracer deployment facilitate comprehensive measurements in karst region, notable for their marked spatial variability.

6. Conclusions

In this study, we developed a tracer-aided conceptual runoff model that employs temperature as a tracer within a karst catchment framework, integrating water and heat transport dynamics across various landscape compartments. Utilizing this model within the characteristic karst terrain of the Chenqi catchment in Southwest China, our investigation focused on the utility of temperature as an efficient, cost-effective tracer for delineating water fluxes and elucidating water age distributions in karst systems. The model demonstrated a capacity for accurately representing the essential behavior of water flux and temperature across different landscape units within the catchment. Using temperature as a tracer, we simulated the flux age distributions within each conceptual storage, as well as the distributions of water transit times. The modeled water age dynamics captured crucial aspects, including variations in flow pathways, the extent of mixing, and the degree of hydrological connectivity intrinsic to the karst catchment under varying moisture regimes.

Our simulations indicated that the outflow's flux age distributions, based on temperature and isotopic tracers, shared congruent patterns at both the catchment outlet and the HS unit. Notwithstanding, the temperature-based model suggested a pronounced abundance of exceptionally young and old waters within the outflow, insinuating a potential overestimation of the extremities in age distribution by utilizing temperature within tracer-aided modeling. The transit time distribution patterns, informed by temperature, closely align with those indicated by isotopic analyses. However, temperature-based simulations inferred a more considerable segment of precipitation being rapidly mobilized through fast flow conduits. According to our simulations, approximately 31 % of inflowing precipitation exited the catchment as streamflow within a span of three years, pointing to a substantial quantity of rainfall being sequestered in the aquifer or lost to evapotranspiration.

Although the application of temperature as a tracer in conceptual models necessitates further refinement in modeling heat transfer processes and warrants extensive validation against a more robust temperature dataset, including aquifer rock temperatures, our research corroborates that readily accessible temperature data can serve as an effective tracer. This approach provides insights into the mechanisms of streamflow generation and water age distributions within karst catchments and potentially extends to non-karstic terrains.

CRediT authorship contribution statement

Zhicai Zhang: Writing – original draft, Software, Methodology, Conceptualization. **Xian Wang:** Validation, Data curation. **Xi Chen:** Writing – review & editing, Project administration, Funding acquisition, Conceptualization. **Yongyu Xie:** Data curation. **Qinbo Cheng:** Methodology, Data curation. **Qing He:** Software. **Tao Peng:** Writing – review

& editing, Resources. **Bo Chen:** Resources, Data curation. **Chris Soulsby:** Writing – review & editing, Formal analysis.

Declaration of competing interest

The authors declare that they have no known competing financial interests or personal relationships that could have appeared to influence the work reported in this paper.

Data availability

Data will be made available on request.

Acknowledgments

Appendix A. Supplementary data

Supplementary data to this article can be found online at https://doi.org/10.1016/j.jhydrol.2024.131947.

References

Asadollahi, M., Stumpp, C., Rinaldo, A., Benettin, P., 2020. Transport and water age dynamics in soils: a comparative study of spatially integrated and spatially explicit models. Water Resour. Res. 56.

Becker, M.W., Georgian, T., Ambrose, H., Siniscalchi, J., Fredrick, K., 2004. Estimating flow and flux of ground water discharge using water temperature and velocity. J. Hydrol. 296.

Benettin, P., Van Der Velde, Y., Van Der Zee, S.E.A.T.M., Rinaldo, A., Botter, G., 2013. Chloride circulation in a lowland catchment and the formulation of transport by travel time distributions. Water Resour. Res. 49.

Benettin, P., Soulsby, C., Birkel, C., Tetzlaff, D., Botter, G., Rinaldo, A., 2017. Using SAS functions and high-resolution isotope data to unravel travel time distributions in headwater catchments. Water Resour. Res. 53, 1864–1878.

Birkel, C., Duvert, C., Correa, A., Munksgaard, N.C., Maher, D.T., Hutley, L.B., 2020. Tracer-aided modeling in the low-relief, wet-dry tropics suggests water ages and DOC export are driven by seasonal wetlands and deep groundwater. Water Resour. Res. 56.

Birkel, C., Soulsby, C., Tetzlaff, D., Dunn, S., Spezia, L., 2012. High-frequency storm event isotope sampling reveals time-variant transit time distributions and influence of diurnal cycles. Hydrol. Process. 26.

Borriero, A., Kumar, R., Nguyen, T. V., Fleckenstein, J.H., Lutz, S.R., 2023. Uncertainty in water transit time estimation with StorAge Selection functions and tracer data interpolation. Hydrol. Earth Syst. Sci. 27.

Botter, G., 2012. Catchment mixing processes and travel time distributions. Water Resour. Res. 48.

Botter, G., Bertuzzo, E., Rinaldo, A. 2011. Catchment residence and travel time distributions: The master equation. Geophys. Res. Lett.

Brookfield, A.E., Macpherson, G.L., Covington, M.D., 2017. Effects of changing meteoric precipitation patterns on groundwater temperature in karst environments. Groundwater 55.

Capell, R., Tetzlaff, D., Soulsby, C., 2012. Can time domain and source area tracers reduce uncertainty in rainfall-runoff models in larger heterogeneous catchments? Water Resour. Res. 48.

Chen, X., Zhang, Z., Soulsby, C., Cheng, Q., Binley, A., Jiang, R., Tao, M., 2018. Characterizing the heterogeneity of karst critical zone and its hydrological function: an integrated approach. Hydrol. Process. 32, 2932–2946.

Cheng, Q., Chen, X., Tao, M., Binley, A., 2019. Characterization of karst structures using quasi-3D electrical resistivity tomography. Environ Earth Sci. 78.

Chi, G., Xing, L., Xing, X., Li, C., Dong, F., 2020. Seepage characteristics of karst water system using temperature tracer technique. Earth. Space. Sci. 7.

Covington, M.D., Luhmann, A.J., Gabrovek, F., Saar, M.O., Wicks, C.M., 2011. Mechanisms of heat exchange between water and rock in karst conduits. Water Resour. Res. 47.

Covington, M.D., Luhmann, A.J., Wicks, C.M., Saar, M.O., 2012. Process length scales and longitudinal damping in karst conduits. J. Geophys. Res.- Earth Surf. 117.

Domínguez-Villar, D., Cukrov, N., Krklec, K., 2018. Temperature as a tracer of hydrological dynamics in an anchialine cave system with a submarine spring. Hydrogeol. J. 26.

Duan, Y., 2015. Experimental study on testing and variation of soil thermophysical parameters. Taiyuan University of Technology, Taiyuan, China in Chinese.

Fan, X.F., 2003. A summary on physical property parameters in southeastern Guizhou. Guizhou Geology 20 (2), 83–91 in Chinese.

Fu, Z., Chen, H., Xu, Q., Jia, J., Wang, S., Wang, K., 2016. Role of epikarst in near-surface hydrological processes in a soil mantled subtropical dolomite karst slope: Implications of field rainfall simulation experiments. Hydrol. Process. 30.

Genthon, P., Bataille, A., Fromant, A., D'Hulst, D., Bourges, F., 2005. Temperature as a marker for karstic waters hydrodynamics. Inferences from 1 year recording at la Peyrére cave (Ariège, France). J. Hydrol. 311.

Gooseff, M.N., McGlynn, B.L., 2005. A stream tracer technique employing ionic tracers and specific conductance data applied to the Maimai catchment, New Zealand. Hydrol Process 19.

Gou, J.F., Qu, S.M., Shi, P., Guan, H., Yang, H., Zhang, Z.C., Liu, J.T., Su, Z.G., 2023. Comparison of transit time models for exploring seasonal variation of preferential flow in a Moso bamboo watershed. J. Hydrol. 626.

Haag, I., Luce, A., 2008. The integrated water balance and water temperature model LARSIM-WT. Hydrol. Process. 22.

Harman, C.J., 2015. Time-variable transit time distributions and transport: Theory and application to storage-dependent transport of chloride in a watershed. Water Resour. Res. 51, 1–30.

Harman, C.J., Sivapalan, M., Kumar, P., 2009. Power law catchment-scale recessions arising from heterogeneous linear small-scale dynamics. Water Resour. Res. 45.

Hrachowitz, M., Savenije, H., Bogaard, T.A., Tetzlaff, D., Soulsby, C., 2013. What can flux tracking teach us about water age distribution patterns and their temporal dynamics? Hydrol. Earth Syst. Sci. 17, 533–564.

Husic, A., Fox, J., Adams, E., Ford, W., Agouridis, C., Currens, J., Backus, J., 2019. Nitrate pathways, processes, and timing in an agricultural karst system: development and application of a numerical model. Water Resour. Res. 55, 2079–2103.

Jackson, F.L., Malcolm, I.A., Hannah, D.M., 2016. Anovel approach for designing large-scale river temperature monitoring networks. Hydrol. Res. 47, 569–590.

Kelleher, C., Ward, A., Knapp, J.L.A., Blaen, P.J., Kurz, M.J., Drummond, J.D., Zarnetske, J.P., Hannah, D.M., Mendoza-Lera, C., Schmadel, N.M., Datry, T., Lewandowski, J., Milner, A.M., Krause, S., 2019. Exploring Tracer Information and Model Framework Trade-Offs to Improve Estimation of Stream Transient Storage Processes. Water Resour Res 55.

Kirchner, J.W., Feng, X., Neal, C., 2000. Fractal stream chemistry and its implications for contaminant transport in catchments. Nature 403, 524–527.

Kirchner, J.W., Feng, X., Neal, C., Robson, A.J., 2004. The fine structure of water-quality dynamics: the (high-frequency) wave of the future. Hydrol. Process. 18, 1353–1359.

Kling, H., Fuchs, M., Paulin, M., 2012. Runoff conditions in the upper Danube basin under an ensemble of climate change scenarios. J. Hydrol. 424–425.

Kwon, Y., Koo, B.K., 2017. Development and evaluation of the soil and water temperature model (SWTM) for rural catchments. J. Hydrol. 553.

Lazo, P.X., Mosquera, G.M., Cárdenas, I., Segura, C., Crespo, P., 2023. Flow partitioning modelling using high-resolution electrical conductivity data during variable flow conditions in a tropical montane catchment. J. Hydrol. 617.

Li, G., Chen, X., Zhang, Z., Wang, L., Soulsby, C., 2022. Effects of passive-storage conceptualization on modeling hydrological function and isotope dynamics in the flow system of a cockpit karst landscape. Hydrol. Earth Syst. Sci. 26.

Luhmann, A.J., Covington, M.D., Alexander, S.C., Chai, S.Y., Schwartz, B.F., Groten, J.T., Alexander, E.C., 2012. Comparing conservative and nonconservative tracers in karst and using them to estimate flow path geometry. J. Hydrol. 448–449, 201–211.

Luo, M., Wan, L., Liao, C., Jakada, H., Zhou, H., 2023. Geographic and transport controls of temperature response in karst springs. J. Hydrol. 623.

McDonnell, J.J., Beven, K., 2014. Debates-The future of hydrological sciences: a (common) path forward? A call to action aimed at understanding velocities, celerities and residence time distributions of the headwater hydrograph. Water Resour. Res. 50, 5342–5350.

Morales-Marín, L.A., Sanyal, P.R., Kadowaki, H., Li, Z., Rokaya, P., Lindenschmidt, K.E., 2019. A hydrological and water temperature modelling framework to simulate the timing of river freeze-up and ice-cover breakup in large-scale catchments. Environ. Modell. Software 114.

Ouellet, V., Secretan, Y., St-Hilaire, A., Morin, J., 2014. Water temperature modelling in a controlled environment: Comparative study of heat budget equations. Hydrol. Process. 28.

Qiu, H., Blaen, P., Comer-Warner, S., Hannah, D.M., Krause, S., Phanikumar, M.S., 2019. Evaluating a coupled phenology-surface energy balance model to understand stream-subsurface temperature dynamics in a mixed-use farmland catchment. Water Resour. Res. 55, 1675–1697.

Rinaldo, A., Benettin, P., Harman, C.J., Hrachowitz, M., McGuire, K.J., Van Der Velde, Y., Bertuzzo, E., Botter, G., 2015. Storage selection functions: a coherent framework for quantifying how catchments store and release water and solutes. Water Resour Res. 51, 4840–4847.

Rusjan, S., Sapač, K., Petrič, M., Lojen, S., Bezak, N., 2019. Identifying the hydrological behavior of a complex karst system using stable isotopes. J. Hydrol. 577, 123956.

Serène, L., Batiot-Guilhe, C., Mazzilli, N., Emblanch, C., Babic, M., Dupont, J., Simler, R., Blanc, M., Massonnat, G., 2022. Transit Time index (TTi) as an adaptation of the humification index to illustrate transit time differences in karst hydrosystems: application to the karst springs of the Fontaine de Vaucluse system (southeastern France). Hydrol. Earth Syst. Sci. 26, 5035–5049.

Simon, N., Bour, O., Faucheux, M., Lavenant, N., Le Lay, H., Fovet, O., Thomas, Z., Longuevergne, L., 2022. Combining passive and active distributed temperature sensing measurements to locate and quantify groundwater discharge variability into a headwater stream. Hydrol. Earth Syst. Sci. 26.

Sjöberg, Y., Jan, A., Painter, S.L., Coon, E.T., Carey, M.P., O'Donnell, J.A., Koch, J.C., 2021. Permafrost promotes shallow groundwater flow and warmer headwater streams. Water Resour. Res. 57.

Song, X.Q., Jiang, M., Peng, Q., Xiong, P.W., 2019. Thermal property parameters and influencing factor analysis of main rock strata in Guizhou province. Acta. Geological Sinica. 93 (8), 2092–2103 in Chinese.

Soulsby, C., Birkel, C., Geris, J., Dick, J., Tunaley, C., Tetzlaff, D., 2015. Stream water age distributions controlled by storage dynamics and nonlinear hydrologic connectivity: modeling with high-resolution isotope data. Water Resour. Res. 51, 7759–7776.

Sprenger, M., Tetzlaff, D., Soulsby, C., 2017. Soil water stable isotopes reveal evaporation dynamics at the soil-plant-atmosphere interface of the critical zone. Hydrol. Earth Syst. Sci. 21.

Sprenger, M., Tetzlaff, D., Buttle, J., Laudon, H., Leistert, H., Mitchell, C.P.J., Snelgrove, J., Weiler, M., Soulsby, C., 2018. Measuring and modeling stable isotopes of mobile and bulk soil water. Vadose Zone J. 17.

van der Velde, Y., Heidbüchel, I., Lyon, S.W., Nyberg, L., Rodhe, A., Bishop, K., Troch, P. A., 2015. Consequences of mixing assumptions for time-variable travel time distributions. Hydrol. Process. 29, 3460–3474.

Wang, Y., Lu, Y., Horton, R., Ren, T., 2019. Specific Heat Capacity of Soil Solids: Influences of Clay Content, Organic Matter, and Tightly Bound Water. Soil Sci. Soc. Am. J. 83.

Wang, Z.-J., Li, S.-L., Yue, F.-J., Qin, C.-Q., Buckerfield, S., Zeng, J., 2020. Rainfall driven nitrate transport in agricultural karst surface river system: insight from high resolution hydrochemistry and nitrate isotopes. Agric. Ecosyst. Environ. 291, 106787.

Wang Y.Y, 2008. Research on the Characteristics of the Epikarst Developing in Puding Region, Guizhou Province, Southwestern China, Nanjing University, Nanjing, P.R. China. (in Chinese).

Webb, B.W., Hannah, D.M., Moore, R.D., Brown, L.E., Nobilis, F., 2008. Recent advances in stream and river temperature research. Hydrol. Process. https://doi.org/10.1002/hyp.6994.

Williams, P.W., 2008. The role of the epikarst in karst and cave hydrogeology: a review. Int. J. Speleol. https://doi.org/10.5038/1827-806X.37.1.1.

Wilusz, D.C., Harman, C.J., Ball, W.P., Maxwell, R.M., Buda, A.R., 2020. Using Particle Tracking to Understand Flow Paths, Age Distributions, and the Paradoxical Origins of the Inverse Storage Effect in an Experimental Catchment. Water Resour. Res. 56.

Wu, S., Tetzlaff, D., Goldhammer, T., Freymueller, J., Soulsby, C., 2022. Tracer-aided identification of hydrological and biogeochemical controls on in-stream water quality in a riparian wetland. Water Res. 222.

Wu, S., Tetzlaff, D., Yang, X.Q., Smith, A., Soulsby, C., 2023. Integrating tracers and soft data into multi-criteria calibration: implications from distributed modeling in a riparian wetland. Water Resour. Res. 59.

Yang, X., Tetzlaff, D., Müller, C., Knöller, K., Borchardt, D., Soulsby, C., 2023. Upscaling tracer-aided ecohydrological modeling to larger catchments: implications for process representation and heterogeneity in landscape organization. Water Resour. Res. 59.

Yearsley, J.R., Sun, N., Baptiste, M., Nijssen, B., 2019. Assessing the impacts of hydrologic and land use alterations on water temperature in the Farmington River basin in Connecticut. Hydrol. Earth Syst. Sci. 23.

Yue, F.-J., Li, S.-L., Waldron, S., Wang, Z.-J., Oliver, D.M., Chen, X., Liu, C.-Q., 2020. Rainfall and conduit drainage combine to accelerate nitrate loss from a karst agroecosystem: Insights from stable isotope tracing and high-frequency nitrate sensing. Water Res. 186, 116388.

Zhang, Z., Chen, X., Ghadouani, A., Shi, P., 2011. Modelling hydrological processes influenced by soil, rock and vegetation in a small karst basin of southwest China. Hydrol. Process. 25, 2456–2470.

Zhang, Z., Chen, Xi, Chen, Xunhong, Shi, P., 2013. Quantifying time lag of epikarst-spring hydrograph response to rainfall using correlation and spectral analyses. Hydrogeol. J. 21, 1619–1631.

Zhang, Z., Chen, X., Cheng, Q., Soulsby, C., 2019. Storage dynamics, hydrological connectivity and flux ages in a karst catchment: conceptual modelling using stable isotopes. Hydrol. Earth Syst. Sci. 23, 51–71.

Zhang, R., Chen, X., Zhang, Z., Soulsby, C., 2020a. Using hysteretic behaviour and hydrograph classification to identify hydrological function across the "hillslope–depression–stream" continuum in a karst catchment. Hydrol. Process 34, 3464–3480.

Zhang, Z., Chen, X., Cheng, Q., Li, S., Yue, F., Peng, T., Waldron, S., Oliver, D.M., Soulsby, C., 2020b. Coupled hydrological and biogeochemical modelling of nitrogen transport in the karst critical zone. Sci. Total Environ. 732, 138902.

Zhang, Z., Chen, X., Cheng, Q., Soulsby, C., 2020c. Characterizing the variability of transit time distributions and young water fractions in karst catchments using flux tracking. Hydrol. Process. 34, 3156–3174.

Zhang, Z., Chen, X., Cheng, Q., Soulsby, C., 2021a. Using StorAge Selection (SAS) functions to understand flow paths and age distributions in contrasting karst groundwater systems. J. Hydrol. 602, 126785.

Zhang, Z., Chen, X., Li, S., Yue, F., Cheng, Q., Peng, T., Soulsby, C., 2021b. Linking nitrate dynamics to water age in underground conduit flows in a karst catchment. J. Hydrol. 596, 125699.

Zhang, Z., Kane, D.L., Hinzman, L.D., 2000. Development and application of a spatially-distributed arctic hydrological and thermal process model (ARHYTHM). Hydrol. Process. 14.